

Stabilizing the Q-Gradient Field for Policy Smoothness in Actor–Critic

Jeong Woon Lee ^{* 1} Kyoleen Kwak ^{* 2} Daeho Kim ^{* 1} Hyoseok Hwang ^{† 1}

Abstract

Policies learned via continuous actor-critic methods often exhibit erratic, high-frequency oscillations, making them unsuitable for physical deployment. Current approaches attempt to enforce smoothness by directly regularizing the policy’s output. We argue that this approach treats the symptom rather than the cause. In this work, we theoretically establish that policy non-smoothness is fundamentally governed by the differential geometry of the critic. By applying implicit differentiation to the actor-critic objective, we prove that the sensitivity of the optimal policy is bounded by the ratio of the Q-function’s mixed-partial derivative (noise sensitivity) to its action-space curvature (signal distinctness). To empirically validate this theoretical insight, we introduce *Policy-Aware Value-field Equalization* (PAVE), a critic-centric regularization framework that treats the critic as a scalar field and *stabilizes* its induced action-gradient field. PAVE rectifies the learning signal by minimizing the Q-gradient volatility while preserving local curvature. Experimental results demonstrate that PAVE achieves smoothness and robustness comparable to policy-side smoothness regularization methods, while maintaining competitive task performance, without modifying the actor.

1. Introduction

Deep reinforcement learning (RL) has become a standard approach for continuous control, with strong results across locomotion and manipulation benchmarks (Hwangbo et al., 2019; Levine et al., 2016) using actor–critic methods such as Soft Actor-Critic (SAC) (Haarnoja et al., 2018) and Twin Delayed Deep Deterministic Policy Gradient (TD3) (Fujimoto et al., 2018). However, a persistent gap between simulation success and real deployment remains action in-

¹Department of Software Convergence, Kyung Hee University
²Department of Artificial intelligence, Kyung Hee University.
 Correspondence to: Hyoseok Hwang <hyoseok@khu.ac.kr>.

stability: trained policies often exhibit high-frequency oscillations and “jerky” control signals (Chen et al., 2021; Mysore et al., 2021). In physical systems, such oscillations translate into higher energy consumption, accelerated actuator wear, vibration-induced fatigue, and potential safety issues; (Inman, 2013; de la Presilla et al., 2023) they also degrade human-perceived quality even when task return is high (Chen et al., 2021).

To mitigate this, the dominant paradigm has been to explicitly constrain the policy network. This body of work includes adding regularization terms to the actor’s loss function to enforce spatial or temporal consistency (Mysore et al., 2021; Kobayashi, 2022; Lee et al., 2024), and more recently, aligning actions with trajectory-based predictions to capture system dynamics (Kwak & Hwang, 2026). Alternatively, architectural approaches modify the policy network structure to enforce Lipschitz continuity (Takase et al., 2022; Song et al., 2023). Theoretically, these methods share a common goal of reducing the policy network’s Lipschitz constant (Song et al., 2023).

While these approaches mitigate action oscillations, we contend that they address the *symptom* rather than the *cause*. Even under strong regularization, if the underlying Q-function remains noisy, the resulting policy gradients continue to drive the actor in erratic directions. This introduces a conflict during optimization: the actor faces competing objectives—minimizing the smoothing penalty versus ascending a volatile learning signal. Consequently, the policy is compelled to diverge from the return-maximizing manifold to satisfy smoothness constraints, compromising task performance.

We propose a fundamental shift in perspective: from forcing the actor to be smooth, to inducing smoothness via a stable learning signal. We argue that the root cause of policy non-smoothness lies deeper, within the geometric structure of the critic’s value function that guides the actor. This dynamic is central to continuous actor-critic frameworks, which have become the standard for continuous control (Lillicrap et al., 2015; Fujimoto et al., 2018; Haarnoja et al., 2018). In this paradigm, the policy is updated by ascending the gradient of the Q-function with respect to the action, $\nabla_a Q(s, a)$. This Q-gradient field serves as the learning signal, defining the direction of steepest ascent for policy improvement. If this

field is geometrically unstable—where the gradient direction flips drastically with infinitesimal state perturbations—the actor is fundamentally misled. Since the policy is optimized to follow these gradients, diverging optimization directions at neighboring states compel the actor to produce disparate actions, directly manifesting as high-frequency oscillations.

To formalize this idea, we analyze the optimal policy induced by the critic via implicit differentiation. This theoretical examination reveals that the sensitivity of the optimal action is strictly governed by the interplay of two geometric properties: (i) the mixed state-action Hessian $\nabla_{sa}^2 Q$ and (ii) the conditioning of the action Hessian $\nabla_{aa}^2 Q$. The mixed Hessian $\nabla_{sa}^2 Q$ quantifies the volatility of the learning signal, representing how rapidly the direction of steepest ascent rotates with small state variations. Meanwhile, the action Hessian $\nabla_{aa}^2 Q$ dictates the curvature of the peak itself; a flat landscape creates an ill-conditioned maximization problem where the optimal action becomes hypersensitive to negligible shifts.

This observation suggests a different strategy: rather than constraining the actor to compensate for an irregular learning signal, we propose to directly regularize the geometry of the Q-function itself. Intuitively, if the value field is smooth and well-conditioned over the state-action manifold, the induced action-gradient field becomes stable by construction. Crucially, this approach differs from naively smoothing the value function, which might obscure necessary control information. By minimizing noise sensitivity ($\nabla_{sa}^2 Q$) while explicitly preserving signal curvature ($\nabla_{aa}^2 Q$), we ensure that smooth policies emerge naturally without sacrificing the distinctness of the optimal action.

To empirically validate this theoretical insight, we introduce *Policy-Aware Value-field Equalization* (PAVE), a critic-centric regularization framework that treats the critic as a scalar field over the state-action manifold and *stabilizes* its induced action-gradient field. PAVE combines (i) *Mixed-Partial Regularization* to bound state-induced changes of the action-gradient (ii) *Vector Field Consistency* based on Fisher divergence to align Q-gradient fields across temporal transitions, and (iii) *Curvature Preservation* to maintain well-defined local maxima. Our experimental results show that, by modifying the critic’s geometric structure alone, PAVE achieves action smoothness comparable to policy-side regularization methods, without any modification to the actor. Our contributions are as follows:

- We identify the critic’s geometry as the primary source of action instability. By applying implicit differentiation, we rigorously prove that policy sensitivity is fundamentally governed by the mixed-partial derivatives and action curvature of the Q-function.
- We propose PAVE, a critic-centric regularization frame-

work designed to validate our theory by stabilizing the Q-gradient field rather than constraining the actor.

- We provide empirical evidence that *paving* the value landscape yields enhanced control smoothness and robustness while maintaining competitive task scores, thereby validating our hypothesis that critic geometry is the fundamental driver of action stability.

2. Related Work

2.1. Policy-side smoothness regularization

A prevalent strategy for mitigating action oscillations involves explicitly constraining the policy network to limit its Lipschitz constant. This is primarily achieved by augmenting the actor’s objective function with regularization terms. A seminal work in this domain, Conditioning for Action Policy Smoothness (CAPS) (Mysore et al., 2021), penalizes differences between temporally consecutive actions and spatially adjacent states sampled from a fixed Gaussian neighborhood. To improve adaptability, Local Lipschitz Continuous Constraint (L2C2) (Kobayashi, 2022) dynamically adjusts the spatial neighborhood radius based on the state. Gradient-based CAPS (Grad-CAPS) (Lee et al., 2024) regularizes action gradients to suppress high-frequency zigzagging. Most recently, ASAP (Kwak & Hwang, 2026) refines spatial regularization by utilizing transition-induced distributions and aligning actions with predictions from preceding states, supplemented by second-order temporal penalties. Complementary to loss-based penalties, architectural methods modify the neural network structure to intrinsically satisfy Lipschitz continuity. Spectral Normalization (Gogianu et al., 2021; Bjorck et al., 2021) has been adapted to RL to stabilize training by bounding the policy’s Lipschitz constant. More specialized architectures like LipsNet (Song et al., 2023) ensure global and local smoothness via Multi-dimensional Gradient Normalization (MGN), directly constraining the Jacobian’s operator norm. This approach has been extended in LipsNet++ (Song et al., 2025) to decouple high-frequency noise from control signals using Fourier-based filtering. Unlike these prior works that focused on constraining the policy, we propose a paradigm shift that addresses the root cause of instability by focusing directly on the geometry of the critic.

2.2. Critic geometry and gradient regularization

Stabilizing learning signals via gradient/Jacobian regularization has been explored broadly (Sokolić et al., 2017; Roth et al., 2017). In RL, these methods are typically applied to improve robustness or training stability, but they do not explicitly connect critic differential geometry to policy smoothness (Gogianu et al., 2021). Our work focuses on the specific geometric terms that govern the state-sensitivity

of the critic-induced greedy policy (mixed partials and action curvature), and proposes targeted regularization that minimizes volatility while explicitly preserving useful local discrimination. In our approach, this can be interpreted as stabilizing and equalizing the induced *Q-gradient field* that the actor follows during learning.

2.3. Score matching and Fisher divergence

Score matching aligns gradients of log-densities without partition functions (Hyvärinen & Dayan, 2005). Modern score-based generative modeling learns smooth score fields with related objectives (Song & Ermon, 2019). We adapt this perspective to RL by treating $\nabla_a Q$ as a vector field whose temporal consistency can be regularized, yielding more stable actor update directions along trajectories.

3. Preliminary

We formulate the continuous control problem as a Markov Decision Process (MDP) defined by the tuple $(\mathcal{S}, \mathcal{A}, P, r, \gamma)$, where \mathcal{S} and \mathcal{A} denote the continuous state and action spaces, $P : \mathcal{S} \times \mathcal{A} \rightarrow \mathcal{P}(\mathcal{S})$ is the transition dynamics, $r : \mathcal{S} \times \mathcal{A} \rightarrow \mathbb{R}$ is the reward function, and $\gamma \in [0, 1]$ is the discount factor. The objective is to learn a policy $\pi : \mathcal{S} \rightarrow \mathcal{P}(\mathcal{A})$ that maximizes the expected return $\mathbb{E}[\sum_{t=0}^{\infty} \gamma^t r(s_t, a_t)]$.

Modern actor-critic methods learn a critic $Q_\theta(s, a)$ to approximate the action-value function and update a parameterized policy π_ϕ by ascending the Q-function's gradient. For deterministic actors, such as TD3 (Fujimoto et al., 2018), the update follows the Deterministic Policy Gradient (DPG) (Silver et al., 2014):

$$\nabla_\phi J(\phi) = \mathbb{E}_{s \sim \mathcal{D}} [\nabla_a Q_\theta(s, a)|_{a=\pi_\phi(s)} \nabla_\phi \pi_\phi(s)], \quad (1)$$

where \mathcal{D} represents the replay buffer. Similarly, for stochastic actors exemplified by SAC (Haarnoja et al., 2018), although the objective includes an entropy term, the policy update is fundamentally driven by the same gradient flow $\nabla_a Q_\theta(s, a)$ via the reparameterization trick.

In both paradigms, the actor attempts to approximate the implicit greedy policy $a^*(s) = \arg \max_a Q_\theta(s, a)$. Consequently, the geometric properties of the critic directly dictate the stability of the actor. We treat the gradient $\nabla_a Q_\theta(s, \cdot)$ as a vector field over the state-action manifold; stabilizing the geometry of Q-gradient field is the core focus of PAVE.

4. Theoretical Analysis: The Geometry of Policy Sensitivity

To remediate the fundamental origin of action instability in actor-critic methods, it is imperative to analyze how the differential geometry of the value function dic-

tates the behavior of the induced policy. In this section, we rigorously derive the sensitivity of the greedy policy $a^*(s) = \arg \max_a Q_\theta(s, a)$ with respect to state perturbations. By integrating the Implicit Function Theorem (IFT) into our analysis, we explicitly demonstrate that the smoothness of the policy is governed by specific Hessian terms of the critic.

4.1. Implicit Policy Definition and Sensitivity Derivation

In the actor-critic paradigm, the actor $\pi_\phi(s)$ is optimized to approximate the maximizer of the Q-function. Even in continuous control settings where the actor is a neural network, its gradient update direction is fundamentally driven by $\nabla_a Q_\theta(s, \pi_\phi(s))$. Consequently, the geometric regularity of the explicit maximizer $a^*(s) = \arg \max_a Q_\theta(s, a)$ imposes a fundamental limit on the policy: the parameterized actor π_ϕ cannot exceed the smoothness of a^* without deviating from the optimal action and incurring a performance penalty. We formally characterize the local sensitivity of the optimal action via the following lemma.

Lemma 4.1 (Implicit Policy Jacobian). *Let $Q_\theta : \mathcal{S} \times \mathcal{A} \rightarrow \mathbb{R}$ be a twice continuously differentiable function. Assume that for a given state s , $a^*(s)$ corresponds to a strict local maximum and is an interior point of \mathcal{A} , such that the action Hessian $\nabla_{aa}^2 Q_\theta(s, a^*(s))$ is negative definite. Then, the sensitivity of the optimal action with respect to the state, denoted by the policy Jacobian $J_\pi(s) = \nabla_s a^*(s)$, is analytically given by:*

$$J_\pi(s) = - [\nabla_{aa}^2 Q_\theta(s, a^*(s))]^{-1} \nabla_{sa}^2 Q_\theta(s, a^*(s)). \quad (2)$$

Proof. Since $a^*(s)$ is an interior extremum, it must satisfy the first-order optimality condition $\nabla_a Q_\theta(s, a^*(s)) = 0$. We consider this gradient as a vector-valued mapping $G(s, a(s)) = 0$. Applying the total derivative with respect to s via the chain rule yields:

$$\begin{aligned} \frac{d}{ds} G(s, a^*(s)) &= \nabla_{sa}^2 Q_\theta(s, a^*(s)) \\ &+ \nabla_{aa}^2 Q_\theta(s, a^*(s)) \nabla_s a^*(s) = 0. \end{aligned} \quad (3)$$

Given the strict concavity assumption, the Hessian $\nabla_{aa}^2 Q_\theta(s, a^*(s))$ is invertible. Rearranging the terms, we obtain:

$$\nabla_{aa}^2 Q_\theta(s, a^*(s)) \nabla_s a^*(s) = -\nabla_{sa}^2 Q_\theta(s, a^*(s)). \quad (4)$$

Pre-multiplying by the inverse Hessian $[\nabla_{aa}^2 Q_\theta(s, a^*(s))]^{-1}$ yields the expression in Equation (2). \square

Equation (2) offers a crucial geometric intuition: policy sensitivity is the product of the *inverse curvature* and the

mixed-partial coupling. Intuitively, $\nabla_{sa}^2 Q_\theta$ acts as a forcing term that dictates how the ascent direction shifts, while $[\nabla_{aa}^2 Q_\theta]^{-1}$ acts as an amplification factor determined by the landscape's flatness. If the Q-surface is flat (low curvature), the inverse Hessian explodes, rendering the policy hypersensitive to even negligible gradient rotations. This factorization provides the rigorous mathematical basis for our proposed regularization strategy.

4.2. Spectral Bounds on Lipschitz Continuity

We now establish a concrete bound on the Lipschitz constant of the policy by analyzing the spectral norms of the constituent matrices in Lemma 4.1.

Proposition 4.2 (Lipschitz Continuity Bound). *Let $\|\cdot\|_2$ denote the spectral norm. Suppose the mixed partial derivative is bounded by $\|\nabla_{sa}^2 Q_\theta(s, a^*(s))\|_2 \leq M$ and the action Hessian satisfies the strict concavity condition $\lambda_{\max}(\nabla_{aa}^2 Q_\theta(s, a^*(s))) \leq -\mu < 0$ (where $\lambda_{\max}(\cdot)$ denotes the maximum eigenvalue). Then, the induced greedy policy is Lipschitz continuous with a constant L satisfying:*

$$\|a^*(s) - a^*(s')\|_2 \leq L\|s - s'\|_2, \quad \text{where } L \leq \frac{M}{\mu}. \quad (5)$$

Proof. We analyze the spectral norm of the policy Jacobian derived in Theorem 4.1. Leveraging the sub-multiplicative property of the spectral norm, we have:

$$\|J_\pi(s)\|_2 \leq \left\| \left[\nabla_{aa}^2 Q_\theta(s, a^*(s)) \right]^{-1} \right\|_2 \cdot \left\| \nabla_{sa}^2 Q_\theta(s, a^*(s)) \right\|_2. \quad (6)$$

1. Curvature Bound: The assumption $\lambda_{\max}(\nabla_{aa}^2 Q_\theta(s, a^*(s))) \leq -\mu$ implies that the spectrum of the Hessian lies entirely in $(-\infty, -\mu]$. Consequently, the eigenvalues of the inverse Hessian are bounded in magnitude by $1/\mu$. Thus:

$$\left\| \left[\nabla_{aa}^2 Q_\theta \right]^{-1} \right\|_2 = \frac{1}{|\lambda_{\max}(\nabla_{aa}^2 Q_\theta(s, a^*(s)))|} \leq \frac{1}{\mu}. \quad (7)$$

2. Mixed-Partial Bound: By hypothesis, the sensitivity of the gradient field to state variations is bounded by $\|\nabla_{sa}^2 Q_\theta\|_2 \leq M$.

Substituting these bounds, we define the Lipschitz constant L as the supremum of the policy Jacobian norm:

$$L \triangleq \sup_s \|\nabla_s a^*(s)\|_2 \leq \frac{M}{\mu}. \quad (8)$$

Finally, applying the Mean Value Inequality for vector-

valued differentiable functions, for any pair of states s, s' :

$$\begin{aligned} & \|a^*(s) - a^*(s')\|_2 \\ & \leq \left(\sup_z \|\nabla_s a^*(z)\|_2 \right) \|s - s'\|_2 \\ & = L\|s - s'\|_2 \leq \frac{M}{\mu}\|s - s'\|_2. \end{aligned} \quad (9)$$

This confirms that the policy is Lipschitz continuous with constant $L \leq M/\mu$. \square

Theoretical Implication. The derived bound $L \leq M/\mu$ highlights a critical insight: simply minimizing the gradient variance (reducing M) is insufficient if the curvature μ also vanishes. Conventional regularization methods often inadvertently flatten the Q-landscape, driving $\mu \rightarrow 0$, which can theoretically explode the sensitivity term $\|(\nabla_{aa}^2 Q_\theta(\cdot))^{-1}\|$. PAVE is explicitly formulated to minimize M while ensuring μ remains strictly bounded away from zero.

5. PAVE: Policy-Aware Value-field Equalization

We introduce PAVE, a critic-centric framework designed to explicitly enforce the geometric stability conditions derived in Section 4. Instead of constraining the actor, PAVE directly regularizes the value field to minimize the Lipschitz bound $L \leq M/\mu$ and enforce trajectory consistency. This is achieved via three synergistic objectives: (1) suppressing noise sensitivity (M) via *Mixed-Partial Regularization*, (2) aligning temporal vector fields via *Vector Field Consistency*, and (3) preserving curvature (μ) via *Curvature Preservation* to prevent geometric collapse.

5.1. Mixed-Partial Regularization (MPR)

To minimize the numerator M in Equation (5), it is necessary to suppress the magnitude of the mixed partial derivatives $\nabla_{sa}^2 Q_\theta$. However, explicit computation of the Hessian imposes a computational complexity of $\mathcal{O}(d^2)$, which is prohibitive for online RL.

We circumvent this by employing a finite-difference approximation grounded in Taylor expansion. Consider the perturbation of the action-gradient $\nabla_a Q_\theta$ induced by a small state variation ϵ :

$$\nabla_a Q_\theta(s + \epsilon, a) = \nabla_a Q_\theta(s, a) + \nabla_{sa}^2 Q_\theta(s, a)\epsilon + \mathcal{O}(\|\epsilon\|^2). \quad (10)$$

Neglecting higher-order terms, the difference $\|\nabla_a Q_\theta(s + \epsilon, a) - \nabla_a Q_\theta(s, a)\|$ serves as an efficient proxy for the Hessian-vector product $\|\nabla_{sa}^2 Q_\theta(s, a)\epsilon\|$. Accordingly, we

define the Mixed-Partial Regularization (MPR) objective as:

$$\mathcal{L}_{\text{MPR}}(\theta) = \mathbb{E}_{\substack{(s,a) \sim \mathcal{D} \\ \epsilon \sim \mathcal{N}(0, \sigma^2 I)}} \left[\left\| \nabla_a Q_\theta(s + \epsilon, a) - \nabla_a Q_\theta(s, a) \right\|_2^2 \right]. \quad (11)$$

Minimizing this objective enforces local invariance of the vector field $\nabla_a Q_\theta$ with respect to state perturbations, effectively compressing the spectral norm M and widening the region of attraction for the optimal action.

Formal Justification. We further provide a mathematical justification for why minimizing Equation (11) bounds the spectral norm M . By substituting the linear approximation into the objective and taking the expectation over the isotropic Gaussian noise ϵ , we obtain:

$$\begin{aligned} \mathcal{L}_{\text{MPR}} &\approx \mathbb{E}_\epsilon \left[\left\| \nabla_{sa}^2 Q_\theta(s, a) \epsilon \right\|_2^2 \right] \\ &= \mathbb{E}_\epsilon \left[\epsilon^\top (\nabla_{sa}^2 Q_\theta(s, a))^\top \nabla_{sa}^2 Q_\theta(s, a) \epsilon \right] \\ &= \sigma^2 \left\| \nabla_{sa}^2 Q_\theta(s, a) \right\|_F^2. \end{aligned} \quad (12)$$

Since the spectral norm is upper-bounded by the Frobenius norm ($\|A\|_2 \leq \|A\|_F$), minimizing \mathcal{L}_{MPR} suppresses the upper bound of M , thereby enforcing the desired Lipschitz continuity.

5.2. Vector Field Consistency (VFC)

While MPR enforces spatial smoothness via isotropic perturbations, stable robotic control necessitates *temporal* coherence along trajectories. Ideally, the learning signal driving the actor should not exhibit high-frequency fluctuations between consecutive time steps (Kwak & Hwang, 2026).

To formalize this, we draw inspiration from Score Matching (Hyvärinen & Dayan, 2005). By interpreting the gradient $\nabla_a Q_\theta(s, a)$ as the score function of an implicit Boltzmann policy $p(a|s) \propto \exp(Q_\theta(s, a))$, we frame temporal stability as minimizing the distributional shift of the policy. Specifically, we minimize the Euclidean distance between the score fields induced by consecutive states s_t and s_{t+1} , which is analogous to minimizing the Fisher Divergence:

$$\mathcal{L}_{\text{VFC}}(\theta) = \mathbb{E}_{(s_t, a_t, s_{t+1}) \sim \mathcal{D}} \left[\left\| \nabla_a Q_\theta(s_t, a_t) - \nabla_a Q_\theta(s_{t+1}, a_t) \right\|_2^2 \right]. \quad (13)$$

This objective aligns the direction of policy improvement along the temporal dimension, effectively mitigating the “chattering” effect caused by conflicting gradients at adjacent time steps.

Algorithm 1 PAVE: Policy-Aware Value-field Equalization

```

1: Input: Hyperparameters  $\lambda_1, \lambda_2, \lambda_3$ , noise scale  $\sigma$ , margin  $\delta$ 
2: Initialize: Critic  $\theta$ , Actor  $\phi$ , Target networks  $\theta', \phi'$ , Replay buffer  $\mathcal{D}$ 
3: for each environment step do
4:   Sample action  $a_t \sim \pi_\phi(s_t)$  (with exploration noise)
5:   Execute  $a_t$ , observe  $r_t, s_{t+1}$ , store  $(s_t, a_t, r_t, s_{t+1})$  in  $\mathcal{D}$ 
6:   for each gradient step do
7:     Sample batch  $\mathcal{B} = \{(s, a, r, s')\} \sim \mathcal{D}$ 
8:     // 1. Standard TD Learning
9:     Compute  $\mathcal{L}_{\text{TD}}(\theta)$  using targets  $\theta', \phi'$ 
10:    // 2. Mixed-Partial Regularization (MPR)
11:    Sample perturbations  $\epsilon \sim \mathcal{N}(\mathbf{0}, \sigma^2 I)$ 
12:     $\mathcal{L}_{\text{MPR}} \leftarrow \frac{1}{|\mathcal{B}|} \sum \left\| \nabla_a Q_\theta(s + \epsilon, a) - \nabla_a Q_\theta(s, a) \right\|_2^2$ 
13:    // 3. Vector Field Consistency (VFC)
14:     $\mathcal{L}_{\text{VFC}} \leftarrow \frac{1}{|\mathcal{B}|} \sum \left\| \nabla_a Q_\theta(s, a) - \nabla_a Q_\theta(s', a) \right\|_2^2$ 
15:    // 4. Curvature Preservation (Curv)
16:    Sample vectors  $v \sim \text{Rademacher}(|\mathcal{A}|)$ 
17:     $Tr_{\text{est}} \leftarrow v^\top \nabla_{aa}^2 Q_\theta(s, a) v$ 
18:     $\mathcal{L}_{\text{Curv}} \leftarrow \frac{1}{|\mathcal{B}|} \sum \max(0, Tr_{\text{est}} + \delta)$ 
19:    // 5. Joint Update
20:     $\mathcal{L}_{\text{Total}} \leftarrow \mathcal{L}_{\text{TD}} + \lambda_1 \mathcal{L}_{\text{MPR}} + \lambda_2 \mathcal{L}_{\text{VFC}} + \lambda_3 \mathcal{L}_{\text{Curv}}$ 
21:     $\theta \leftarrow \theta - \eta \nabla_\theta \mathcal{L}_{\text{Total}}$ 
22:    Update actor  $\phi$  via  $\nabla_\phi J(\phi)$ 
23:  end for
24: end for

```

Formal Justification. Similar to MPR, VFC also serves to bound the mixed-partial term M , but specifically along the manifold of system dynamics. Considering the first-order expansion $s_{t+1} \approx s_t + \Delta s_t$, the objective approximates the directional Hessian norm:

$$\begin{aligned} \left\| \nabla_a Q_\theta(s_{t+1}, a_t) - \nabla_a Q_\theta(s_t, a_t) \right\|_2^2 &\approx \\ \left\| \nabla_{sa}^2 Q_\theta(s_t, a_t) \Delta s_t \right\|_2^2. \end{aligned} \quad (14)$$

While MPR reduces M globally, VFC specifically suppresses the sensitivity of the optimal action to state transitions imposed by the environment dynamics ($\nabla_{sa}^2 Q_\theta(\Delta s_t)$), ensuring kinematic realizability.

5.3. Curvature Preservation (Curv)

Minimizing \mathcal{L}_{MPR} in isolation introduces a pathological risk: the neural network may collapse the Q-function to a trivial flat plane (i.e., $\nabla_a Q_\theta \approx \mathbf{0}, \forall s, a$) to satisfy the smoothness constraint. As established in Proposition 4.2, if Q_θ becomes flat, the term $\|(\nabla_{aa}^2 Q_\theta(s, a))^{-1}\|$ diverges, paradoxically amplifying policy sensitivity.

To preclude this “over-smoothing” collapse, we must enforce the geometric constraint that the curvature μ remains

Table 1. Cumulative return (*re*) and smoothness score (*sm*) on Gymnasium benchmark under TD3 setting. Higher *re* and lower *sm* are better. Bold indicates best, and underlined the second-best, per environment. Standard deviations shown in parentheses.

Method	LunarLander		Pendulum		Reacher		Ant		Hopper		Walker	
	<i>re</i> ↑	<i>sm</i> ↓	<i>re</i> ↑	<i>sm</i> ↓	<i>re</i> ↑	<i>sm</i> ↓	<i>re</i> ↑	<i>sm</i> ↓	<i>re</i> ↑	<i>sm</i> ↓	<i>re</i> ↑	<i>sm</i> ↓
TD3 Base	244.5 (58.1)	1.438 (0.777)	-168.7 (77.5)	2.276 (0.995)	-3.59 (1.34)	0.055 (0.015)	4859 (1014)	2.089 (0.190)	3424 (393)	3.286 (0.359)	4868 (742)	1.976 (0.287)
CAPS	252.2 (66.0)	0.880 (0.422)	-175.7 (80.2)	0.381 (0.170)	-3.65 (1.34)	0.051 (0.015)	4390 (1421)	2.033 (0.256)	3303 (670)	2.275 (0.529)	4714 (759)	1.963 (0.283)
GRAD	206.7 (118.6)	1.055 (0.791)	-169.3 (77.0)	0.575 (0.152)	-3.61 (1.32)	0.044 (0.012)	5110 (885)	1.866 (0.081)	3345 (570)	1.615 (0.211)	4412 (695)	1.434 (0.240)
ASAP	228.9 (55.7)	1.574 (0.704)	-165.7 (74.5)	1.056 (0.361)	-3.58 (1.33)	0.053 (0.014)	4617 (1096)	2.019 (0.308)	3552 (61)	2.192 (0.334)	4434 (667)	1.859 (0.165)
PAVE	264.5 (24.9)	0.541 (0.290)	-167.6 (77.5)	0.351 (0.118)	-4.02 (1.34)	0.039 (0.013)	4649 (1443)	1.768 (0.315)	3305 (461)	0.950 (0.285)	5563 (451)	1.272 (0.172)

positive. We propose Curvature Preservation (Curv), which penalizes the trace of the action Hessian if it fails to maintain sufficient concavity:

$$\mathcal{L}_{\text{Curv}} = \mathbb{E}_{\substack{(s,a) \sim \mathcal{D} \\ v \sim p(v)}} \left[\max \left(0, v^\top \nabla_{aa}^2 Q_\theta(s, a) v + \delta \right) \right], \quad (15)$$

where $\delta > 0$ defines the minimum required sharpness. To ensure computational efficiency, we employ Hutchinson's trace estimator with random Rademacher vectors v . Note that we utilize SiLU activation in the critic to ensure C^2 continuity for valid Hessian computation.

Formal Justification. This regularizer explicitly targets the denominator μ in the Lipschitz bound $L \leq M/\mu$. By penalizing projected curvature values $v^\top \nabla_{aa}^2 Q_\theta(s, a) v$ that exceed $-\delta$, this objective stochastically enforces the spectral constraint $\lambda_{\max}(\nabla_{aa}^2 Q_\theta(\cdot)) \leq -\delta$. This prevents the maximum eigenvalue from approaching zero, guaranteeing that the inverse Hessian norm remains bounded and precluding sensitivity explosion.

5.4. Total Objective Formulation

The composite objective function for the critic parameter θ is formulated as a weighted sum of the TD error and the proposed geometric regularizers:

$$\mathcal{L}(\theta) = \mathcal{L}_{\text{TD}} + \lambda_1 \mathcal{L}_{\text{MPR}} + \lambda_2 \mathcal{L}_{\text{VFC}} + \lambda_3 \mathcal{L}_{\text{Curv}}, \quad (16)$$

where \mathcal{L}_{TD} denotes the standard temporal-difference regression objective. The complete training procedure is summarized in Algorithm 1. Crucially, these geometric regularizers are applied solely as auxiliary losses to the critic. Consequently, the actor update mechanism remains unchanged, utilizing unmodified standard policy gradients while benefiting significantly from the paved, well-conditioned Q-gradient landscape.

6. Empirical Analysis

6.1. Experimental Setup

Experiments were conducted using Gymnasium (Towers et al., 2024) and MuJoCo (Todorov et al., 2012) across six environments: *LunarLanderContinuous-v2*, *Pendulum-v1*, *Reacher-v2*, *Ant-v5*, *Hopper-v5*, and *Walker2d-v5*. This suite spans low-dimensional stabilization to high-dimensional articulated locomotion, providing a diverse testbed for evaluating both task performance and policy smoothness. For evaluation metrics, we use Cumulative Return (*re*) to assess task competency and Smoothness Score (*sm*) to quantify action oscillations. The latter is a spectral smoothness metric derived via Fast Fourier Transform (FFT) analysis, following established protocols (Mysore et al., 2021; Christmann et al., 2024). We built the codebase on top of Stable-Baselines3 (Raffin et al., 2021), building upon the implementation provided in (Kwak & Hwang, 2026). We integrated PAVE into two widely-used off-policy algorithms, Twin Delayed Deep Deterministic policy gradient (TD3) (Fujimoto et al., 2018) and Soft Actor-Critic (SAC) (Haarnoja et al., 2018). Regarding network architectures, we retained the original ReLU activation for BASE, CAPS, Grad-CAPS, and ASAP. For PAVE, we adopted SiLU (Elfwing et al., 2018); as a smooth approximation of ReLU, this ensures valid Hessian computation for curvature optimization while maintaining a fair and competitive performance baseline. We trained our method with five independent random seeds.

6.2. Analysis of Geometric Regularization

In TD3 setting detailed in Table 1, our results validated the theoretical premise that stabilizing the Q-gradient field can naturally induce policy smoothness without hindering performance. While baseline methods often exhibited a trade-off where improved smoothness came at the cost of reduced returns, PAVE effectively maintained or improved task per-

Table 2. Cumulative return (re) and smoothness score (sm) on Gymnasium benchmark under SAC setting. Higher re and lower sm are better. Bold indicates best, and underlined the second-best, per environment. Standard deviations shown in parentheses.

Method	LunarLander		Pendulum		Reacher		Ant		Hopper		Walker	
	$re \uparrow$	$sm \downarrow$	$re \uparrow$	$sm \downarrow$	$re \uparrow$	$sm \downarrow$	$re \uparrow$	$sm \downarrow$	$re \uparrow$	$sm \downarrow$	$re \uparrow$	$sm \downarrow$
SAC Base	278.8 (19.2)	0.297 (0.069)	<u>-162.5</u> (73.9)	0.460 (0.168)	-3.60 (1.37)	0.053 (0.016)	<u>5226</u> (678)	1.865 (0.101)	<u>3462</u> (25)	0.908 (0.091)	<u>4755</u> (267)	0.885 (0.152)
CAPS	281.1 (19.9)	0.276 (0.049)	-165.0 (75.8)	<u>0.315</u> (0.107)	-3.70 (1.40)	0.049 (0.014)	4225 (2267)	1.624 (0.552)	3430 (42)	0.745 (0.058)	4567 (653)	0.824 (0.072)
GRAD	280.7 (18.1)	0.228 (0.048)	-161.9 (72.3)	0.357 (0.124)	<u>-3.62</u> (1.33)	0.045 (0.013)	2995 (3178)	<u>1.251</u> (0.501)	3050 (746)	0.501 (0.063)	4596 (255)	0.591 (0.072)
ASAP	280.8 (20.6)	0.179 (0.037)	-162.7 (73.0)	0.342 (0.110)	-3.66 (1.35)	<u>0.047</u> (0.014)	4642 (1603)	1.148 (0.253)	3455 (222)	0.528 (0.050)	4718 (375)	0.568 (0.067)
PAVE	265.8 (21.4)	0.142 (0.028)	-165.4 (75.5)	0.290 (0.130)	-3.71 (1.31)	0.052 (0.014)	5706 (774)	1.604 (0.146)	3489 (38)	0.556 (0.139)	4954 (250)	0.584 (0.020)

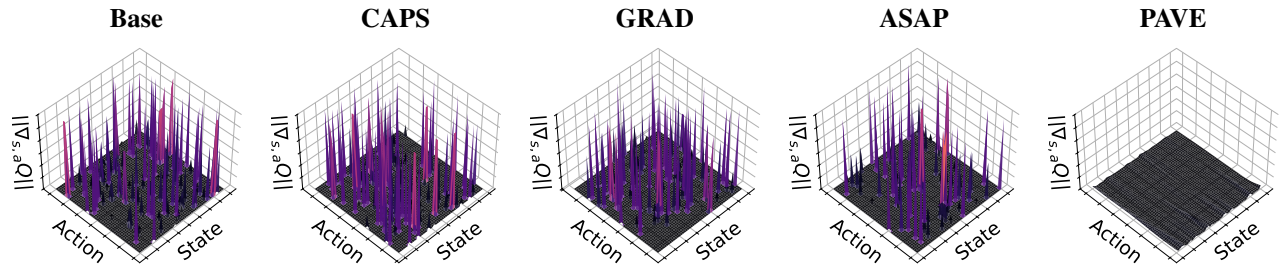


Figure 1. Comprehensive 3D visualization of the mixed-partial Hessian norm $\|\nabla_{sa}^2 Q\|$ in LunarLander. While baseline methods exhibit highly irregular landscapes with sharp spikes, PAVE effectively stabilizes the Q-gradient field, providing a smooth and stable landscape.

formance. Notably, in the Walker task, PAVE achieved the highest cumulative return of 5563 while simultaneously recording the best smoothness score of 1.272. This indicates that for deterministic policies, which are prone to overfitting to sharp gradient irregularities (Matheron et al., 2019), rectifying the critic’s geometry is a highly effective strategy.

The SAC setting presented in Table 2 offered deeper insight into the characteristics of our method. In lower-dimensional tasks such as LunarLander and Reacher, policy-side regularizers like ASAP and GRAD remained competitive, suggesting that direct policy constraints are effective for simpler control manifolds. However, the distinct advantage of PAVE emerged in high-dimensional environments with complex dynamics. In Ant and Walker, PAVE secured higher cumulative returns of 5706 and 4954 respectively compared to the baselines. Crucially, while baselines often sacrificed optimality for smoothness—for instance, ASAP in Ant achieved a lower smoothness score but suffered a significant drop in returns (4642 vs 5706)—PAVE achieved a superior balance. We attribute this to the fact that high-dimensional state-action spaces inherently exhibit more volatile curvature and frequent gradient spikes. In such chaotic landscapes, our critic-centric regularization effectively paved the optimization path, providing a stable learning signal that simple policy constraints fail to capture.

6.3. Qualitative Analysis of the Q-Gradient Field

We qualitatively assessed the learning signal stability by visualizing the mixed-partial Hessian norm $\|\nabla_{sa}^2 Q\|$ in Figure 1 across base TD3 and other regularization methods. The base TD3 and contemporary policy-side regularizers exhibited a “jagged” landscape characterized by numerous sharp spikes, representing a highly unstable learning signal. These jagged landscapes demonstrated that conventional policy-side regularization failed to mitigate the underlying geometric irregularities. In contrast, PAVE effectively paved the gradient field, inducing a flat and consistent landscape. This visualization confirmed that PAVE successfully minimized the mixed-partial volatility (M) as intended by our theoretical objective. A detailed description of the visualization protocol and corresponding plots for all six benchmark environments are provided in Appendix A.

6.4. Robustness to Observation Noise

We evaluated robustness against scale-aware observation noise defined as $\delta \sim \mathcal{U}(-\sigma, \sigma) \odot \sigma_{\text{base}}$. As summarized in Table 3, PAVE exhibited remarkable stability across varying noise levels. Crucially, PAVE demonstrated performance invariance to noise intensity; in the Walker task, the agent maintained nearly identical returns of approximately 5570 even as the noise magnitude increased tenfold

Table 3. Robustness under varying observation noise levels $\sigma \in \{0.01, 0.05, 0.1\}$. We compare the total average return (re) and smoothness score (sm) across various TD3-based regularization methods. Standard deviations shown in parentheses.

Method	LunarLander						Walker					
	0.01		0.05		0.1		0.01		0.05		0.1	
	$re \uparrow$	$sm \downarrow$	$re \uparrow$	$sm \downarrow$	$re \uparrow$	$sm \downarrow$	$re \uparrow$	$sm \downarrow$	$re \uparrow$	$sm \downarrow$	$re \uparrow$	$sm \downarrow$
Base	225.9 (24.0)	1.563 (0.272)	214.9 (32.5)	1.962 (0.264)	169.0 (17.7)	2.517 (0.428)	4860.5 (708.3)	1.981 (0.255)	4903.3 (652.7)	2.155 (0.274)	4866.6 (670.4)	2.395 (0.277)
CAPS	252.5 (22.8)	1.001 (0.168)	223.6 (34.3)	1.222 (0.210)	197.2 (32.9)	1.561 (0.443)	4783.2 (460.0)	2.003 (0.282)	4682.5 (553.8)	2.081 (0.256)	4663.0 (595.2)	2.202 (0.184)
GRAD	238.3 (25.0)	0.997 (0.155)	220.4 (45.8)	1.390 (0.298)	218.1 (27.8)	1.788 (0.311)	4380.7 (713.1)	1.434 (0.223)	4253.8 (773.6)	1.593 (0.199)	4201.4 (811.0)	1.851 (0.205)
ASAP	204.5 (45.1)	1.612 (0.251)	229.7 (18.4)	1.825 (0.175)	202.2 (30.4)	2.308 (0.276)	4434.9 (181.5)	1.892 (0.145)	4493.5 (202.9)	2.018 (0.096)	4403.0 (223.6)	2.230 (0.093)
PAVE	264.4 (6.1)	0.525 (0.055)	244.9 (29.3)	0.897 (0.287)	228.2 (21.4)	1.615 (0.397)	5565.3 (452.3)	1.293 (0.162)	5579.4 (449.2)	1.478 (0.151)	5578.6 (450.0)	1.775 (0.100)

Table 4. Component analysis of each loss component in PAVE. We incrementally add the loss terms to the base TD3 algorithm to demonstrate their individual and combined effects.

Configuration	LunarLander		Walker	
	$re \uparrow$	$sm \downarrow$	$re \uparrow$	$sm \downarrow$
Base	227.8 (74.1)	1.809 (1.311)	4834.3 (423.0)	1.990 (0.208)
$+ \mathcal{L}_{MPR}$	223.6 (74.6)	1.748 (1.187)	4947.2 (486.7)	1.841 (0.191)
$+ \mathcal{L}_{MPR} + \mathcal{L}_{VFC}$	237.4 (58.7)	1.177 (0.461)	4648.2 (291.8)	1.497 (0.241)
$+ \mathcal{L}_{MPR} + \mathcal{L}_{VFC} + \mathcal{L}_{Curv}$	264.5 (24.9)	0.541 (0.290)	5562.9 (451.4)	1.272 (0.172)

from $\sigma = 0.01$ to 0.1 . This indicated that the paved Q-gradient field effectively decoupled input perturbations from action generation. Furthermore, while the smoothness score naturally increased with higher noise, PAVE exhibited a controlled and gradual degradation with scores ranging from 1.29 to 1.77 in the Walker task, whereas baseline methods often suffered from erratic control signal explosions or significant performance collapse under high-noise conditions.

6.5. Component Analysis

We analyzed the contribution of each component via an incremental ablation study. For this analysis, the baseline was modified to incorporate SiLU activation. As shown in Table 4, the addition of \mathcal{L}_{MPR} and \mathcal{L}_{VFC} progressively improved policy smoothness. However, smoothness alone did not guarantee performance; notably, the Walker return dipped to 4648.2. Crucially, the integration of \mathcal{L}_{Curv} was indispensable. It not only recovered and boosted the return to 5562.9 but further enhanced smoothness. This result directly validated our theoretical bound $L \leq M/\mu$ by proving that minimizing volatility alone was insufficient if curvature vanished; by preventing the landscape from flattening, PAVE ensured the inverse Hessian did not act as an amplification

factor for policy sensitivity. We provide a detailed sensitivity analysis, isolating the impact of each regularization coefficient, in Appendix B.

6.6. Complexity Analysis

While PAVE introduces geometric regularizers to stabilize the critic, it is designed to maintain linear computational complexity $\mathcal{O}(k + d)$, where k and d denote state and action dimensions, respectively. Unlike methods requiring explicit Hessian construction ($\mathcal{O}(d^2)$), PAVE utilizes finite difference approximations and Hutchinson’s trace estimator to ensure scalability to high-dimensional tasks. A detailed complexity derivation is provided in Appendix C. As shown in Table 5, PAVE exhibited lower training throughput (FPS) compared to vanilla TD3 and other baselines. However, we emphasize that this overhead is confined to the training phase. Since PAVE does not alter the architecture, the inference speed remains identical to that of the base algorithm.

Table 5. Training Throughput (FPS) Comparison.

Environment	BASE	CAPS	GRAD	ASAP	PAVE
LunarLander	97.5	83.1	78.1	57.8	25.0
Walker	95.8	78.6	69.6	41.0	27.0

7. Conclusion

In this work, we identify the critic’s irregular geometry as the root of policy instability. Using the Implicit Function Theorem, we prove that policy sensitivity is governed by the ratio of the Q-function’s mixed-partial volatility to its curvature. To validate this insight, we propose PAVE to stabilize this geometry. Empirical results confirm that paving the Q-gradient field induces smooth policies without actor constraints, substantiating our hypothesis and the importance of a critic-centric perspective in continuous control.

Impact Statement

This paper presents work whose goal is to advance the field of machine learning. There are many potential societal consequences of our work, none of which we feel must be specifically highlighted here.

References

Bjorck, N., Gomes, C. P., and Weinberger, K. Q. Towards deeper deep reinforcement learning with spectral normalization. *Advances in neural information processing systems*, 34:8242–8255, 2021.

Chen, C., Tang, H., Hao, J., Liu, W., and Meng, Z. Addressing action oscillations through learning policy inertia. In *Proceedings of the AAAI Conference on Artificial Intelligence*, volume 35, pp. 7020–7027, 2021.

Christmann, G., Luo, Y.-S., Mandala, H., and Chen, W.-C. Benchmarking smoothness and reducing high-frequency oscillations in continuous control policies. In *2024 IEEE/RSJ International Conference on Intelligent Robots and Systems (IROS)*, pp. 627–634. IEEE, 2024.

de la Presilla, R., Wandel, S., Stammler, M., Grebe, M., Poll, G., and Glavatskikh, S. Oscillating rolling element bearings: A review of tribotesting and analysis approaches. *Tribology International*, 188:108805, 2023. ISSN 0301-679X. doi: <https://doi.org/10.1016/j.triboint.2023.108805>. URL <https://www.sciencedirect.com/science/article/pii/S0301679X23005935>.

Elfwing, S., Uchibe, E., and Doya, K. Sigmoid-weighted linear units for neural network function approximation in reinforcement learning. *Neural networks*, 107:3–11, 2018.

Fujimoto, S., Hoof, H., and Meger, D. Addressing function approximation error in actor-critic methods. In *International conference on machine learning*, pp. 1587–1596. PMLR, 2018.

Gogianu, F., Berariu, T., Rosca, M. C., Clopath, C., Busoni, L., and Pascanu, R. Spectral normalisation for deep reinforcement learning: an optimisation perspective. In *International Conference on Machine Learning*, pp. 3734–3744. PMLR, 2021.

Haarnoja, T., Zhou, A., Abbeel, P., and Levine, S. Soft actor-critic: Off-policy maximum entropy deep reinforcement learning with a stochastic actor. In *International conference on machine learning*, pp. 1861–1870. Pmlr, 2018.

Hwangbo, J., Lee, J., Dosovitskiy, A., Bellicoso, D., Tsounis, V., Koltun, V., and Hutter, M. Learning agile and dynamic motor skills for legged robots. *Science Robotics*, 4(26):eaau5872, 2019.

Hyvärinen, A. and Dayan, P. Estimation of non-normalized statistical models by score matching. *Journal of Machine Learning Research*, 6(4), 2005.

Inman, D. J. *Engineering Vibration*. Pearson, 4th edition, 2013.

Kobayashi, T. L2c2: Locally lipschitz continuous constraint towards stable and smooth reinforcement learning. In *2022 IEEE/RSJ International Conference on Intelligent Robots and Systems (IROS)*, pp. 4032–4039. IEEE, 2022.

Kwak, K. and Hwang, H. Enhancing control policy smoothness by aligning actions with predictions from preceding states. *arXiv preprint arXiv:2601.18479*, 2026.

Lee, I., Cao, H.-G., Dao, C.-T., Chen, Y.-C., and Wu, I.-C. Gradient-based regularization for action smoothness in robotic control with reinforcement learning. In *2024 IEEE/RSJ International Conference on Intelligent Robots and Systems (IROS)*, pp. 603–610. IEEE, 2024.

Levine, S., Finn, C., Darrell, T., and Abbeel, P. End-to-end training of deep visuomotor policies. *Journal of Machine Learning Research*, 17(39):1–40, 2016.

Lillicrap, T. P., Hunt, J. J., Pritzel, A., Heess, N., Erez, T., Tassa, Y., Silver, D., and Wierstra, D. Continuous control with deep reinforcement learning. *arXiv preprint arXiv:1509.02971*, 2015.

Matheron, G., Perrin, N., and Sigaud, O. The problem with ddpg: understanding failures in deterministic environments with sparse rewards. *arXiv preprint arXiv:1911.11679*, 2019.

Mysore, S., Mabsout, B., Mancuso, R., and Saenko, K. Regularizing action policies for smooth control with reinforcement learning. In *2021 IEEE International Conference on Robotics and Automation (ICRA)*, pp. 1810–1816. IEEE, 2021.

Raffin, A., Hill, A., Gleave, A., Kanervisto, A., Ernestus, M., and Dormann, N. Stable-baselines3: Reliable reinforcement learning implementations. *Journal of Machine Learning Research*, 22(268):1–8, 2021.

Roth, K., Lucchi, A., Nowozin, S., and Hofmann, T. Stabilizing training of generative adversarial networks through regularization. *Advances in neural information processing systems*, 30, 2017.

Silver, D., Lever, G., Heess, N., Degris, T., Wierstra, D., and Riedmiller, M. Deterministic policy gradient algorithms. In *International conference on machine learning*, pp. 387–395. Pmlr, 2014.

Sokolić, J., Giryes, R., Sapiro, G., and Rodrigues, M. R. Robust large margin deep neural networks. *IEEE Transactions on Signal Processing*, 65(16):4265–4280, 2017.

Song, X., Duan, J., Wang, W., Li, S. E., Chen, C., Cheng, B., Zhang, B., Wei, J., and Wang, X. S. Lipsnet: A smooth and robust neural network with adaptive lipschitz constant for high accuracy optimal control. In *International Conference on Machine Learning*, pp. 32253–32272. PMLR, 2023.

Song, X., Chen, L., Liu, T., Wang, W., Wang, Y., Qin, S., Ma, Y., Duan, J., and Li, S. E. Lipsnet++: Unifying filter and controller into a policy network. In *Forty-second International Conference on Machine Learning*, 2025. URL <https://openreview.net/forum?id=KZo2XhcSg6>.

Song, Y. and Ermon, S. Generative modeling by estimating gradients of the data distribution. In Wallach, H., Larochelle, H., Beygelzimer, A., d'Alché-Buc, F., Fox, E., and Garnett, R. (eds.), *Advances in Neural Information Processing Systems*, volume 32. Curran Associates, Inc., 2019. URL https://proceedings.neurips.cc/paper_files/paper/2019/file/3001ef257407d5a371a96dcd947c7d93-Paper.pdf.

Takase, R., Yoshikawa, N., Mariyama, T., and Tsuchiya, T. Stability-certified reinforcement learning control via spectral normalization. *Machine Learning with Applications*, 10:100409, 2022.

Todorov, E., Erez, T., and Tassa, Y. Mujoco: A physics engine for model-based control. In *2012 IEEE/RSJ International Conference on Intelligent Robots and Systems*, pp. 5026–5033. IEEE, 2012. doi: 10.1109/IROS.2012.6386109.

Towers, M., Kwiatkowski, A., Terry, J., et al. Gymnasium: A standard interface for reinforcement learning environments. *arXiv preprint arXiv:2407.17032*, 2024.

A. Extended Analysis and Protocol for Q-Gradient Field Visualization

A.1. Visualization Protocol

To qualitatively assess the geometric stability of the learning signal, we visualized the magnitude of the mixed-partial derivatives.

Dominant Axis Selection. For each environment, we first identified the pair of state dimension s_i and action dimension a_j that exhibited the strongest interaction in the vanilla model. This was defined by scanning all combinations and selecting the pair with the maximum mixed-partial derivative magnitude. By fixing the visualization of all compared algorithms to these “dominant axes” identified from the vanilla baseline, we ensure a fair comparison by focusing on the regions most susceptible to instability.

Numerical Approximation. Since standard neural networks with ReLU or SiLU activations are piecewise linear, their theoretical second-order derivatives are zero almost everywhere. To capture the practical “roughness” that an actor-critic agent encounters during optimization, we utilized a numerical finite-difference approximation:

$$\nabla_{sa}^2 Q(s, a) \approx \frac{\nabla_a Q(s + \epsilon \cdot \mathbf{e}_i, a) - \nabla_a Q(s, a)}{\epsilon} \quad (17)$$

where \mathbf{e}_i is a unit vector in the dominant state dimension and $\epsilon = 10^{-3}$. We swept the dominant state and action dimensions across a range of $[-1.0, 1.0]$ and $[-1.5, 1.5]$ respectively, centered at a reference transition. The resulting norm values were clipped at 300 to facilitate a clear visual comparison of the landscape topologies across different algorithms.

A.2. Full Visualization Results Across Environments

Figure 2 and 3 presented the comparative 3D landscapes of the mixed-partial Hessian norm $\|\nabla_{sa}^2 Q\|$ for all six benchmark environments. This cross-environment evaluation confirmed that the geometric instability of the critic—characterized by high-volatility gradient fields—was a universal phenomenon in standard actor-critic training. Across all tested environments, including LunarLander, Pendulum, Reacher, Ant, Hopper, and Walker, the vanilla and existing policy-side regularizers exhibited noticeable landscape irregularities and a dense population of sharp gradient spikes. These spikes indicated that the steepest ascent direction rotated violently even with infinitesimal state shifts, and notably, current policy-side smoothness regularizers like ASAP failed to mitigate these underlying geometric singularities. In contrast, PAVE demonstrated a consistent ability to remove these erratic spikes and stabilize the landscapes into smooth manifolds across the entire suite of environments.

B. Hyperparameter Sensitivity Analysis

Figure 4 illustrated the impact of varying each effective λ on the Average Return and Smoothness Metric. At excessively high values, the smoothness metric notably deteriorated (dashed orange line increased), accompanied by a sharp decline in returns. This phenomenon directly validates our theoretical bound $L \leq M/\mu$. Minimizing gradient volatility (M) via MPR or VFC in isolation tends to flatten the Q-landscape, driving the action-space curvature (μ , the denominator) toward zero. As the denominator vanishes, the norm of the inverse Hessian $\|\nabla_{aa}^2 Q\|^{-1}$ explodes, paradoxically amplifying policy sensitivity despite the regularization. In contrast, the curvature term (λ_3) demonstrated a critical role in stabilization by strictly lower-bounding μ . It effectively prevented the vanishing gradient problem, ensuring that the inverse Hessian did not act as an amplification factor. The results highlighted that λ_3 acted as a necessary counterbalance, maintaining high returns and stability even when strong smoothness regularization was applied.

C. Theoretical Complexity Analysis

To provide a rigorous assessment of PAVE’s efficiency, we denote the dimensionality of the state space as $k = \dim(\mathcal{S})$ and the action space as $d = \dim(\mathcal{A})$. PAVE is engineered to impose second-order geometric constraints while maintaining linear computational scaling, $\mathcal{O}(k + d)$, avoiding the quadratic costs typically associated with explicit Hessian construction.

C.1. Efficient Geometric Proxies

- **MPR & VFC:** Instead of computing the full mixed-partial Hessian $\nabla_{sa}^2 Q \in \mathbb{R}^{d \times k}$, which incurs a cost of $\mathcal{O}(kd)$, these terms utilize a finite-difference approximation grounded in a Taylor expansion. This requires only two gradient

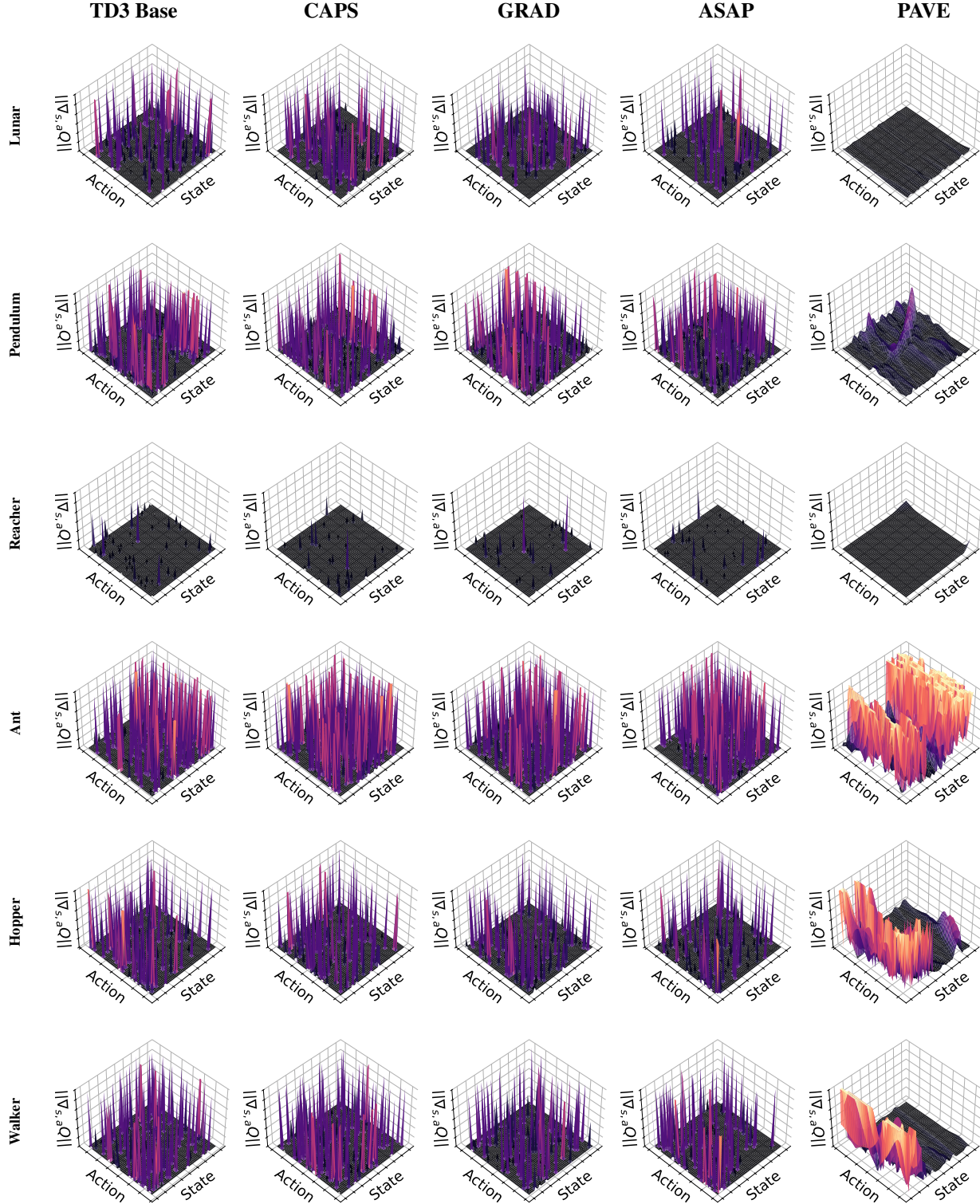


Figure 2. Comprehensive 3D visualization of the mixed-partial Hessian norm $\|\nabla_{sa}^2 Q\|$ across six Gymnasium environments. Each row corresponds to an environment, and each column represents a different stabilization method. While baseline methods exhibit highly irregular landscapes with sharp spikes (indicating an unstable learning signal), PAVE effectively paves the Q-gradient field, providing a smooth and stable landscape. The Z-axis is clipped at 300 for visual clarity and consistent comparison.

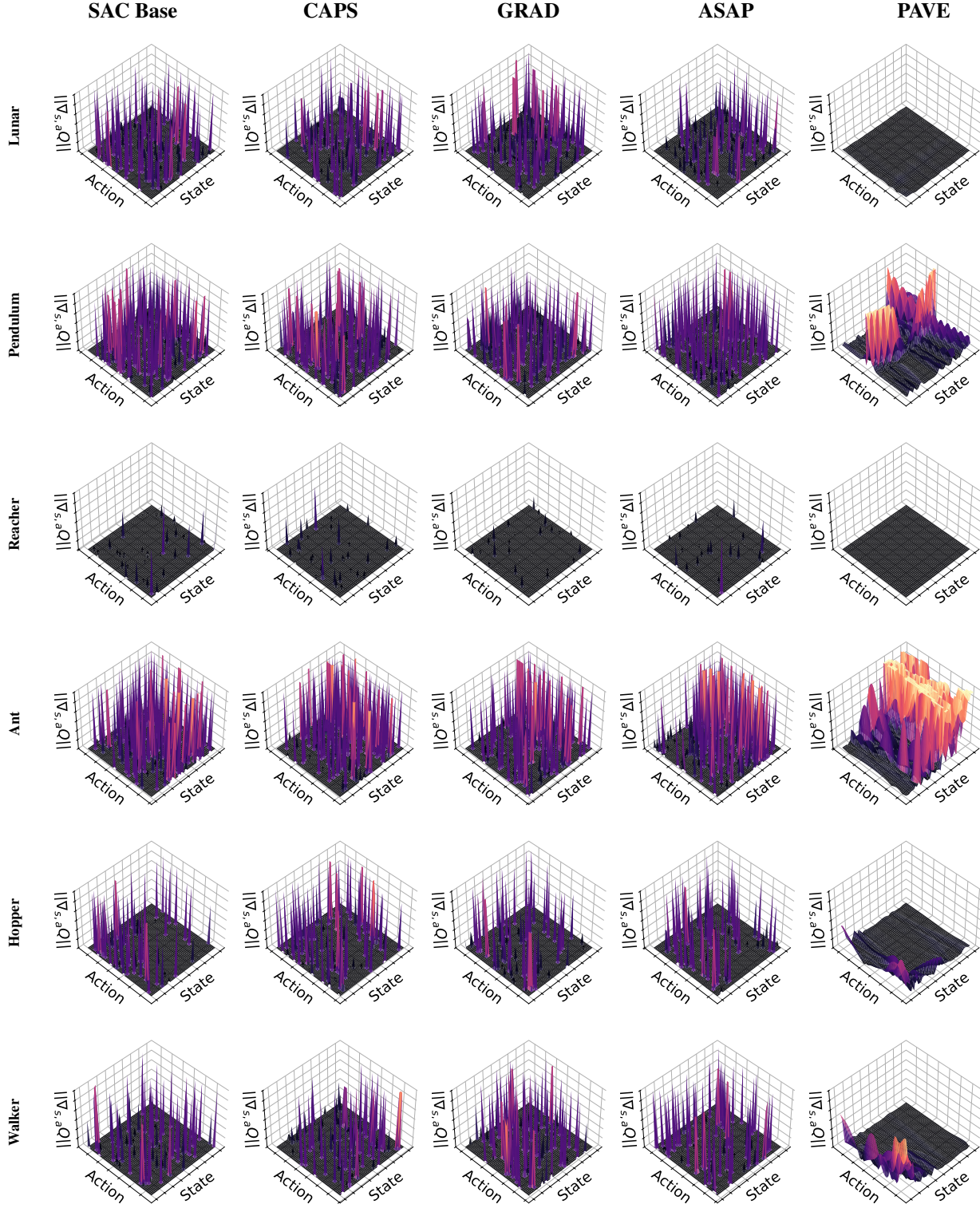


Figure 3. Comprehensive 3D visualization of the mixed-partial Hessian norm $\|\nabla_{sa}^2 Q\|$ across six Gymnasium environments. Each row corresponds to an environment, and each column represents a different stabilization method. While baseline methods exhibit highly irregular landscapes with sharp spikes (indicating an unstable learning signal), PAVE effectively paves the Q-gradient field, providing a smooth and stable landscape. The Z-axis is clipped at 300 for visual clarity and consistent comparison.

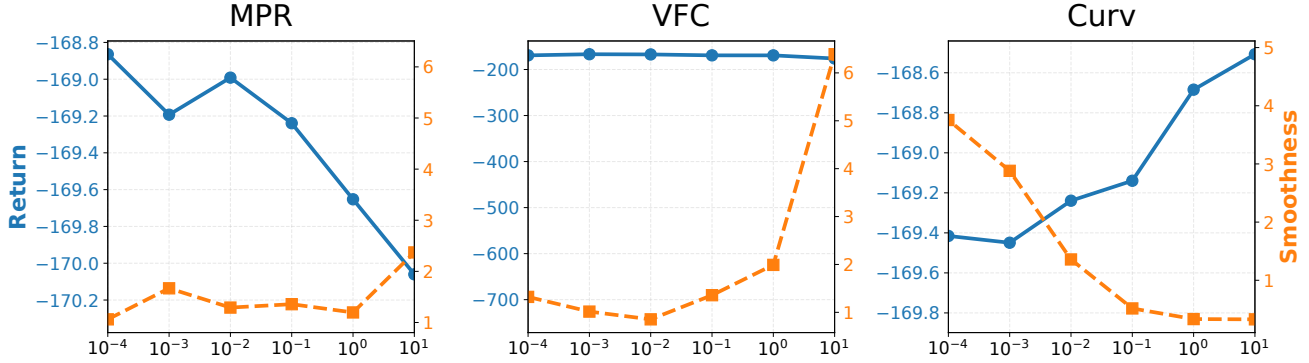


Figure 4. Hyperparameter Sensitivity on Pendulum. For each subplot, only the target parameter was varied while the other two were held fixed at their default settings.

Table 6. Comparison of theoretical computational complexity per update step (k : state dim, d : action dim).

Component	Standard Hessian-based	PAVE
Mixed-Partials ($\nabla_{sa}^2 Q$)	$\mathcal{O}(kd)$	$\mathcal{O}(k + d)$
Action Curvature ($\nabla_{aa}^2 Q$)	$\mathcal{O}(d^2)$	$\mathcal{O}(d)$
Actor Update	$\mathcal{O}(d)$	$\mathcal{O}(d)$
Total Complexity	$\mathcal{O}(kd + d^2)$	$\mathcal{O}(k + d)$

evaluations per update, effectively reducing the complexity to $\mathcal{O}(k + d)$.

- **Curvature Preservation:** The $\mathcal{L}_{\text{Curv}}$ term employs Hutchinson’s trace estimator with random Rademacher vectors to calculate the Hessian-vector product (HVP). This stochastic estimation maintains $\mathcal{O}(d)$ complexity, avoiding the $\mathcal{O}(d^2)$ requirement for full entry-wise computation of $\nabla_{aa}^2 Q$.

C.2. Total Computational Overhead

As summarized in Table 6, PAVE maintains linear scaling across all components. Notably, these geometric regularizers are applied exclusively as auxiliary losses to the critic, leaving the actor update mechanism entirely unchanged. This decoupling ensures the framework’s scalability for high-dimensional articulated control tasks such as the Walker and Ant benchmarks.

D. Visualization of Learning Curves

Figures 5 and 6 presented the learning curves of across various Gymnasium environments. We reported the performance of our proposed method against several baselines including BASE, CAPS, GRAD, and ASAP. Each curve illustrated the mean episodic reward over five independent seeds, with shaded regions representing the standard deviation.

E. Extended Implementation Details

E.1. Report on Hyperparameter Setting

We provide the hyperparameters for each method in the Gymnasium setting in Table 7 and 8.

E.2. Hardware Setting

We utilized distinct computational resources depending on the experimental phase, while ensuring that all comparative algorithms within each benchmark were evaluated on identical hardware settings to guarantee fair comparison. The primary training for all TD3-based methods (including performance and component analysis) was conducted on a server equipped with an Intel Xeon Gold 6226R CPU (@ 2.90GHz) and an NVIDIA GeForce RTX 3090 GPU. Similarly, all SAC-based experiments were executed on a workstation featuring an Intel Xeon Gold 6426Y CPU and an NVIDIA RTX A4000 GPU. In contrast, the robustness analysis and Q-gradient field visualization were performed using pretrained models on a separate

Table 7. Detailed hyperparameters for each method in the Gymnasium-TD3 setting.

Method	Gymnasium Environments					
	LunarLander	Pendulum	Reacher	Ant	Hopper	Walker
CAPS	$\lambda_T = 0.1$	$\lambda_T = 1.0$	$\lambda_T = 0.1$	$\lambda_T = 0.1$	$\lambda_T = 0.1$	$\lambda_T = 0.1$
	$\lambda_S = 0.5$	$\lambda_S = 5.0$	$\lambda_S = 0.5$	$\lambda_S = 0.5$	$\lambda_S = 0.5$	$\lambda_S = 0.5$
	$\sigma = 0.2$	$\sigma = 0.2$	$\sigma = 0.2$	$\sigma = 0.2$	$\sigma = 0.2$	$\sigma = 0.2$
GRAD	$\lambda_T = 1.0$	$\lambda_T = 1.0$	$\lambda_T = 1.0$	$\lambda_T = 1.0$	$\lambda_T = 1.0$	$\lambda_T = 1.0$
ASAP	$\lambda_T = 0.005$	$\lambda_T = 0.005$	$\lambda_T = 0.1$	$\lambda_T = 0.05$	$\lambda_T = 0.07$	$\lambda_T = 0.05$
	$\lambda_S = 0.03$	$\lambda_S = 0.03$	$\lambda_S = 0.1$	$\lambda_S = 0.3$	$\lambda_S = 0.3$	$\lambda_S = 0.3$
	$\lambda_P = 2.0$	$\lambda_P = 2.0$	$\lambda_P = 2.0$	$\lambda_P = 2.0$	$\lambda_P = 2.0$	$\lambda_P = 2.0$
PAVE	$\lambda_1 = 0.1$	$\lambda_1 = 2.0$	$\lambda_1 = 0.1$	$\lambda_1 = 0.1$	$\lambda_1 = 0.1$	$\lambda_1 = 0.1$
	$\lambda_2 = 0.1$	$\lambda_2 = 0.005$	$\lambda_2 = 0.1$	$\lambda_2 = 0.005$	$\lambda_2 = 0.005$	$\lambda_2 = 0.1$
	$\lambda_3 = 0.01$	$\lambda_3 = 2.0$	$\lambda_3 = 0.01$	$\lambda_3 = 0.5$	$\lambda_3 = 0.5$	$\lambda_3 = 0.01$

Table 8. Detailed hyperparameters for each method in the Gymnasium-SAC setting.

Method	Gymnasium Environments					
	LunarLander	Pendulum	Reacher	Ant	Hopper	Walker
CAPS	$\lambda_T = 0.1$	$\lambda_T = 1.0$	$\lambda_T = 0.1$	$\lambda_T = 0.1$	$\lambda_T = 0.1$	$\lambda_T = 0.1$
	$\lambda_S = 0.5$	$\lambda_S = 5.0$	$\lambda_S = 0.5$	$\lambda_S = 0.5$	$\lambda_S = 0.5$	$\lambda_S = 0.5$
	$\sigma = 0.2$	$\sigma = 0.2$	$\sigma = 0.2$	$\sigma = 0.2$	$\sigma = 0.2$	$\sigma = 0.2$
GRAD	$\lambda_T = 1.0$	$\lambda_T = 1.0$	$\lambda_T = 1.0$	$\lambda_T = 1.0$	$\lambda_T = 1.0$	$\lambda_T = 1.0$
ASAP	$\lambda_T = 0.005$	$\lambda_T = 0.005$	$\lambda_T = 0.1$	$\lambda_T = 0.05$	$\lambda_T = 0.07$	$\lambda_T = 0.05$
	$\lambda_S = 0.03$	$\lambda_S = 0.03$	$\lambda_S = 0.1$	$\lambda_S = 0.3$	$\lambda_S = 0.3$	$\lambda_S = 0.3$
	$\lambda_P = 2.0$	$\lambda_P = 2.0$	$\lambda_P = 2.0$	$\lambda_P = 2.0$	$\lambda_P = 2.0$	$\lambda_P = 2.0$
PAVE	$\lambda_1 = 0.1$	$\lambda_1 = 0.1$	$\lambda_1 = 0.1$	$\lambda_1 = 0.1$	$\lambda_1 = 2.0$	$\lambda_1 = 2.0$
	$\lambda_2 = 0.5$	$\lambda_2 = 0.005$	$\lambda_2 = 5e-4$	$\lambda_2 = 5e-4$	$\lambda_2 = 5e-4$	$\lambda_2 = 0.005$
	$\lambda_3 = 0.05$	$\lambda_3 = 0.5$	$\lambda_3 = 1.0$	$\lambda_3 = 1.0$	$\lambda_3 = 3.0$	$\lambda_3 = 2.0$

machine with an AMD Ryzen 7 5800X 8-Core Processor.

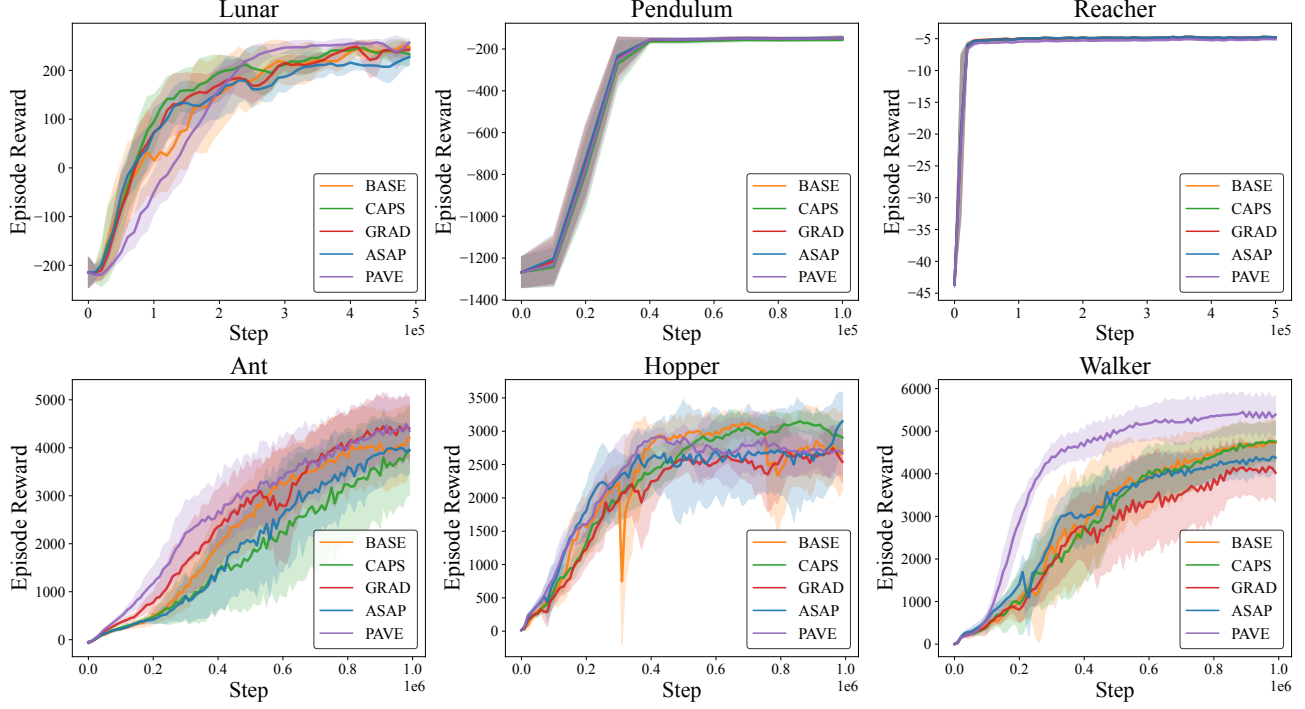


Figure 5. Learning curves of the TD3 algorithm across various Gymnasium environments.

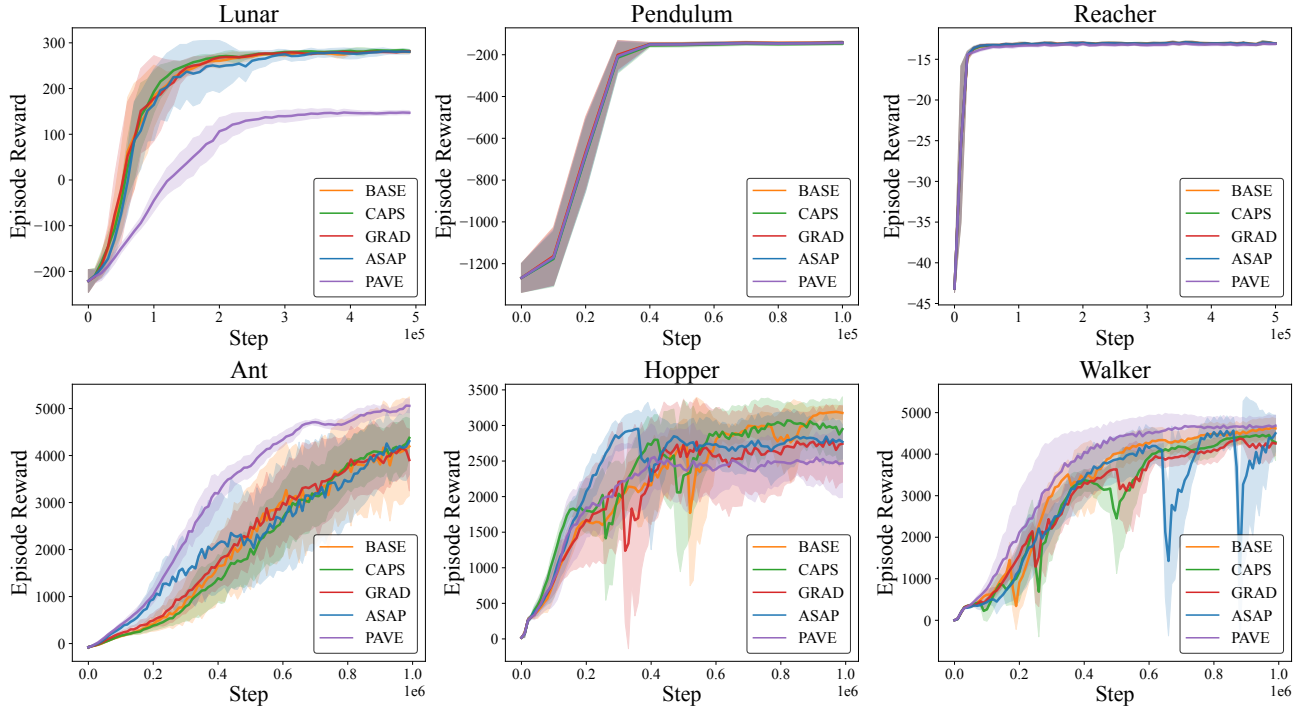


Figure 6. Learning curves of the SAC algorithm across various Gymnasium environments.